CHAPTER 1

INTRODUCTION

There are four parts in this chapter consisting of the background of zinc oxide, tungsten trioxide, flame spray pyrolysis and the characterization techniques.

1.1 Zinc oxide

Zinc oxide is an inorganic compound with the formula ZnO. It usually appears as a white powder. ZnO is often called a II-VI semiconductor because zinc and oxygen belong to the 2nd and 6th groups of the periodic table, respectively. This semiconductor has several advantageous properties: good transparency, high electron mobility, wide bandgap, high electron dissociation, strong room-temperature luminescence, etc. These properties are already used in many applications, for example, photocatalysts, photovoltaics and gas sensors [1-6]. There are 3 forms of crystal structures of ZnO as wurtzite, zinc-blende and rocksalt, as schematically shown in Fig. 1. The wurtzite structure is the most stable at ambient conditions and thus most common. The lattice constants of wurtzite structure are a = 3.25 Å and c = 5.12 Å. The zinc-blende form can be stabilized by growing ZnO on substrates with cubic lattice structure. The calculated lattice constants of zinc-blende structure based on a modern *ab initio* technique are predicted to be 4.60 and 4.619 Å. In both cases, the zinc and oxide centers are tetrahedral. The rocksalt (NaCl-type) structure is only observed at relatively high pressures about 10 Gpa. A high-pressure phase transition from the wurtzite to the rocksalt structure decreases the lattice constant down to the range of 4.271–4.294 Å.

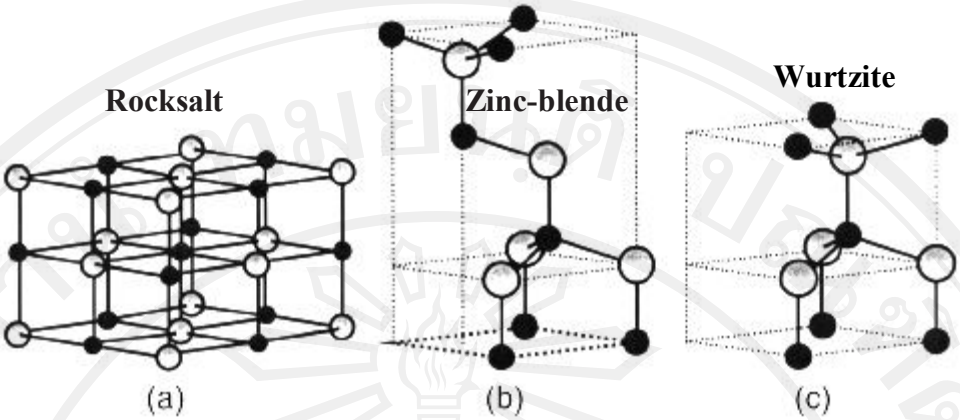

Figure 1.1 Stick and ball representation of ZnO crystal structures: (a) cubic rocksalt, (b) cubic zinc-blende, and (c) hexagonal wurtzite. The shaded gray and black spheres denote Zn and O atoms, respectively. [7]

The common electronic structure of ZnO is wurtzite with space group of C6mc. This structure is based on the hexagonal close-packing (HCP) of anions, with one-half of the tetrahedral sites occupied by the cations. The coordination number of each ion is 4. Let's examine the spatial distribution of tetrahedral sites in HCP to determine how they can be one-half filled, with maximum separation between cations. There are two orientations of tetrahedral sites between close-packed anion layers: those with the apex "up" and those with the apex "down". It can be seen that three are equal numbers of each, and that each forms a hexagonal array with the spacing as the anions. One can therefore fill one-half the total tetrahedral sites with maximum separation by filling only tetrahedral of one orientation. The coordination of anions around cations and of cations around anions is four, as in the zinc-blende structure, thus we can be satisfied that the wurtzite structure also meets the requirements of Pauling's second rule. The unit cell for wurtzite is smaller than that of zinc-blende (it contains only two MX formula units rather than four), so it is more difficult to visualize the interconnections between tetrahedral; they are also linked by corners.

Since each has one-half of the tetrahedral sites filled as well it is reasonable that compounds of one structure often have a polytype of the other. Furthermore, since both atoms are tetrahedrally coordinated in wurtzite, it, like zinc-blande, is the preferred structure of a number of covalent compounds, including AlN and the α phases of SiC.

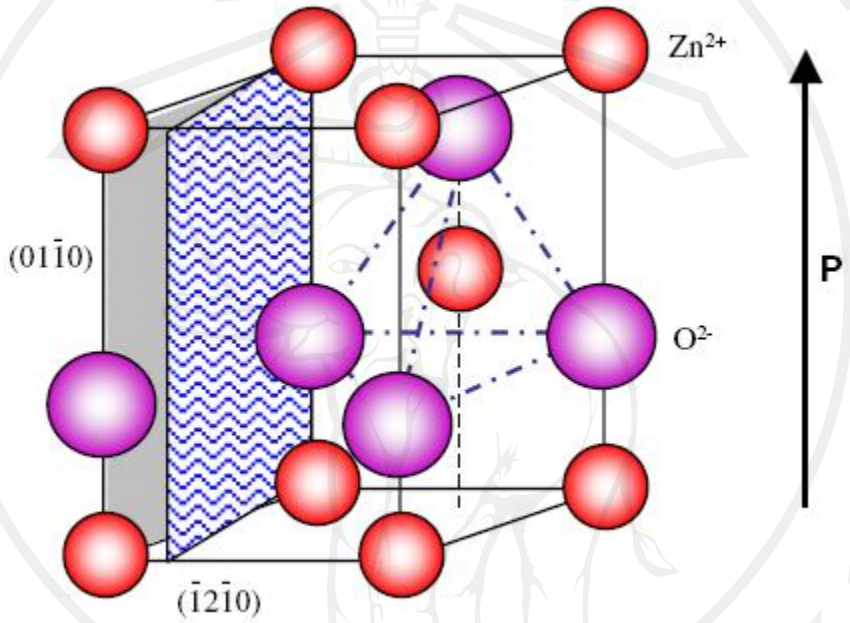

Figure 1.2 The wurtzite structure model of ZnO. The tetrahedral coordination of Zn–O is shown. [8]

The structure of ZnO can be simply described as a number of alternating planes composed of tetrahedrally coordinated O^{2-} and Zn^{2+} ions, attacked alternately along the *c*-axis as shown in Fig 1.2. The tetrahedral coordination in ZnO results in noncentral symmetric structure and consequently piezoelectricity and pyroelectricity. Another important characteristic of ZnO is polar surfaces. The most common polar surface is the basal plane. The oppositely charged ions produce positively charged Zn-(0001) and negatively charged O-$(000\bar{1})$ surfaces, resulting in a normal dipole

moment and spontaneous polarization along the *c*-axis as well as a divergence in surface energy. To maintain a stable structure, the polar surfaces generally have facets or exhibit massive surface reconstructions, but ZnO ±(0001) are exceptions: they are atomically flat, stable and without reconstruction [8]. Efforts to understand the superior stability of the ZnO ±(0001) polar surfaces are at the forefront of research in today's surface physics [8]. The other two most commonly observed facets for ZnO are $\{2\bar{1}\bar{1}0\}$ and {0110}, which are non-polar surfaces and have lower energy than the {0001} facets.

ZnO is a direct band gap semiconductor with E_g = 3.37 eV. The energy gap at room temperature for crystal free donors is 3.2 eV. The band gap of ZnO can be tuned via divalent substitution on the cation site to produce heterostructures. Cd doping can decrease the band gap (to as low as ~3.0 eV), whereas Mg doping can increase the band gap (to as high as ~4.0 eV). Electron doping in nominally undoped ZnO has been attributed to Zn interstitials, oxygen vacancies, or hydrogen. The intrinsic defect levels that lead to n-type doping lie approximately 0.01-0.05 eV below the conduction band. The optical properties of ZnO, studied using photoluminescence, photoconductivity, and absorption reflect the intrinsic direct band gap, a strongly bound exciton state, and gap states arising from point defects. A strong room temperature, near-band-edge UV photoluminescence peak at ~3.2 eV is attributed to an exciton state, as the exciton binding energy is in the order of 60 meV. In addition, visible emission is also observed as a result of defect states. The basic materials parameters of ZnO are shown in Table 1.1 [9-10]. To realize any type of device technology, it is important to have control over the concentration of intentionally introduced impurities, called dopants, which are responsible for the electrical

properties of ZnO. The dopants determine whether the current (and, ultimately, the information processed by the device) is carried by electrons or holes.

Table 1.1 Physical properties of wurtzite ZnO [9-10]

Properties	**Value**
Lattice constants (T = 300 K) a_0 c_0	 0.32469 nm 0.52069 nm
Density	5.606 g/cm^3
Melting point	2248 K
Relative dielectric constant	8.66
Energy gap (crystal free donors)	3.2 eV
Intrinsic carrier concentration	< 10^6 cm^{-3}
Exciton binding Energy	60 meV
Electron effective mass	0.24
Electron mobility (T = 300 K)	200 cm^2/V s
Hole effective mass	0.59
Hole mobility (T = 300 K)	5-50 cm^2/V s

Several preparation techniques of ZnO have been reported in literatures including controlled precipitation method [11], acetate-citrate gelation method [12], polymerized complex method [13], precipitation transformation method [14] and flame spray pyrolysis (FSP) [15]. Among these techniques, FSP is the most outstanding technique because it has many advantages such as low cost precursors, limited agglomeration, aerosolized with O_2, particles can be synthesized in nano-scale

and these nanoparticles can be synthesized in one step as primary particles with high homogeneity [15-18].

1.2 Tungsten trioxide

Tungsten is a transition metal that is easily formed with oxygen to be tungsten trioxide (WO_3) that is the common and stable phase for W-O system [19-20]. The interest in this material goes back to 1837 when Wohler first observed intense metallic luster in $LiWO_3$. He thought the luster was due to the formation of metallic alloys and coined the term ‘‘tungsten bronzes’’. Mott, Sienko, and others performed a significant amount of experimental and theoretical work in the 1950s and 1960s on single crystals of Na–tungsten bronzes because of their unusual electrical properties such as metal–insulator phase transitions and superconductivity at very low temperature [21]. The structural configuration of the crystals of WO_3 is perovskite – like with corner sharing oxygen octahedra enclosing the tungsten atoms, as shown in Figure 1.3. The distortions from the ideal cubic perovskite – like structures results in a number of different WO_3 phases. The amount of distortion is temperature dependent and a WO_3 crystal changes the phase, as cooling down, from tetragonal – orthorhombic – monoclinic – triclinic and finally at -189 °C to a low temperature monoclinic phase. As the displacements are small, there are sometimes difficulties in distinguishing between the different structures. It is tetragonal at temperatures above 740 °C, orthorhombic from 330 to 740 °C, monoclinic from 17 to 330 °C, and triclinic from -50 to 17 °C. The most common structure of WO_3 is monoclinic with space group $P2_1/n$ [22, 23]

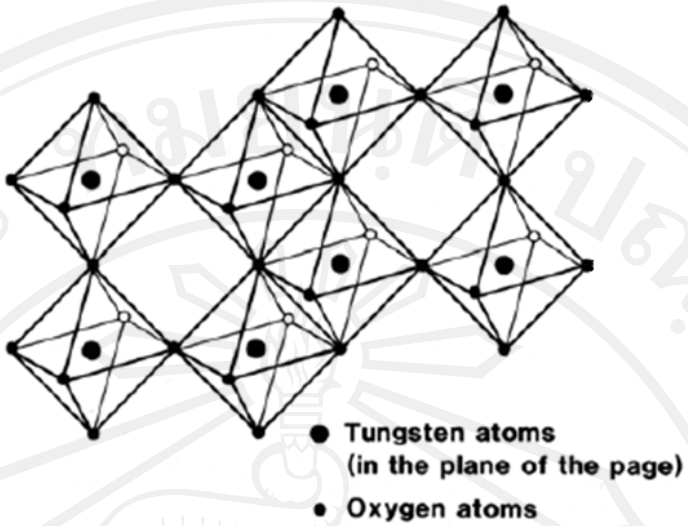

Figure 1.3 Schematic illustration of the arrangement of the octahedra in a slightly substoichiometric WO_3 crystal [22]

WO_3 has many interesting optical, electrical, structural properties so it was used in many applications such as gas sensor [22], photocatalyst [10] and electrochromic devices [20-21].The basic materials parameters of WO_3 are shown in Table 1.2.

Table 1.2 Physical properties of WO_3 [10, 23]

Properties	**Value**
Molar mass	231.84 g/mol
Appearance	Yellow powder
Density	7.16 g/cm^3
Melting point	1473 °C
Boiling point	1700 °C
Crystal structure (T = 300 K)	Monoclinic, mP32, Space group P12$_1$/c1, No 14
energy gap	2.8 eV

There are many techniques for the preparation of fine powder and thin layers of WO_3, for example, cathodic arc deposition [24], gas-phase adsorption in a fluidized-bed reactor [25], laser vaporization [26], chemical vapor deposition from metalorganic precursors [27], electrochemical deposition [28], wet chemical deposition [29], sol–gel process [30] and hydrothermal reactions [31].

1.3 Flame spray pyrolysis (FSP) [15-18, 32-37]

Flame aerosol technology is the key process for large-scale production of nano-structured materials such as carbon blacks, fumed SiO_2 and TiO_2 and to a lesser extent, for specialty chemicals such as Al_2O_3 and ZnO powders. Flame aerosol synthesis is a cost-effective and versatile process for controlled production of nanoparticles [15-18]. Flame spray pyrolysis (FSP) process was systematically investigated using an external-mixing gas-assisted atomizer supported by premixed methane and oxygen flamelets [18, 32]. In flame reactors, the energy of flame is used to drive chemical reactions of precursors resulting in clusters which further grow to nanoparticles by surface growth and/or coagulation and coalescence at high temperature [33]. The advantage of FSP includes the ability to dissolve the precursor directly in the fuel, simplicity of introduction of the precursor into the hot reaction zone (e.g. a flame), and flexibility in using the high-velocity spray jet for rapid quenching of aerosol formation. In general, a flame is used to force chemical reactions of precursor compounds, finally resulting in the formation of clusters, which increase their size to a range of some nanometers by coagulation and sintering. Finally, the nanostructured powders are collected on a filter [18, 32]. The more fuel introduced the higher the flame is and due to that the residence time of particles in the flame is increased. As a consequence time for particle growth is enlarged and bigger

particles are formed [34-35]. The basic steps of particle formation and growth by gas-to-particle conversion in FSP are shown in Figure 1.4.

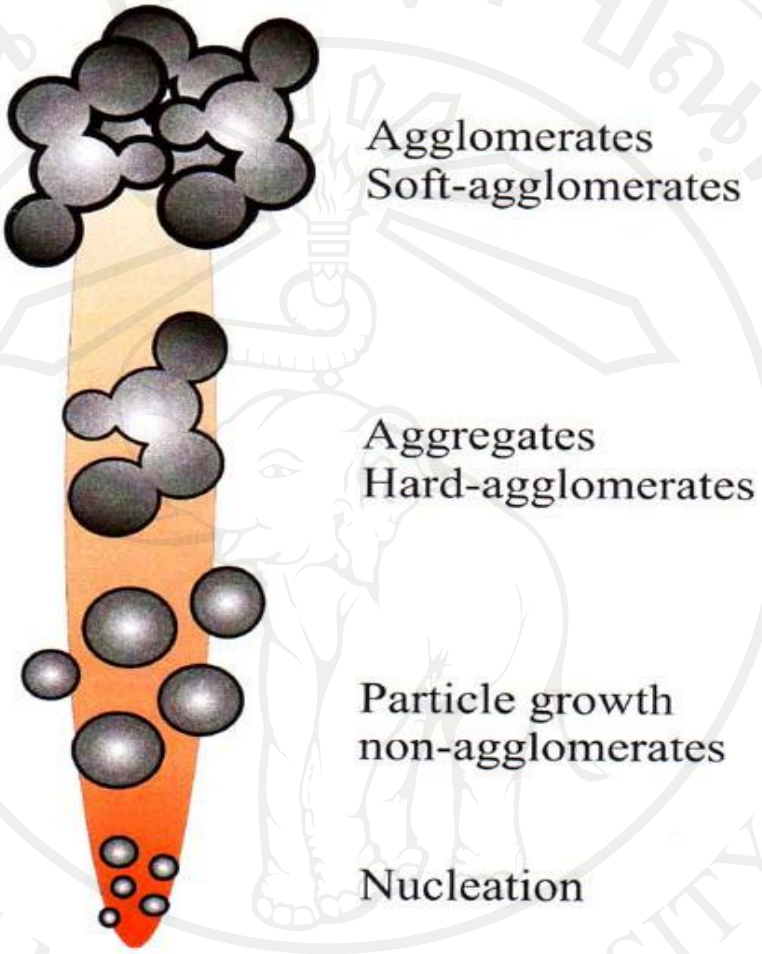

Figure 1.4 The basic steps of particle formation and growth by gas-to-particle conversion in FSP

Moreover, at low oxidant flow rates, the specific surface area increased with increasing oxidant flow rate as the spray flame length was reduced, leading to shorter residence time and allowing less time for particle growth. Using oxygen as oxidant the droplets burn much faster than with air, thus, product particles experience longer residence times at higher temperature [15-18]. The effect of solution feed rate on particles specific surface area and crystalline size was also investigated [15, 17]. The

solution feed rate increased the flame height, and therefore coalescence was enhanced, resulting in large primary particles [15, 17].

In flame reactors the energy of a flame is used to drive chemical reactions of precursor compounds that result in the formation of product molecules, which then nucleate to form particles following the mechanism described earlier. High flame temperatures of 1200 to 3000 K constitute a self-purifying environment for particle synthesis resulting in high-purity powders as for manufacture of optical fiber performs [36]. Even though non-oxide ceramic powders like silicon nitride [16] and tungsten carbide [16] have been synthesized in flame reactors, the production of carbon and metal oxide nanoparticles dominates the field. One distinguishes two types of flame reactor: diffusion and premixed. While premixed flames have the advantage of more uniform radial temperature profiles, diffusion flames are safer to operate (no flashback) and offer flexibility in product quality by controlling the reactant gas composition over broad ranges. Turbulent co-flow diffusion flame reactors are used in industry for large-scale manufacture of ceramic powders. Counterflow diffusion flame reactors, on the other hand, are often used in laboratory studies. The flow along the axial stagnation streamline of a counterflow diffusion flame can be approximated as one-dimensional, facilitating the use of optically-based diagonostics for non-intrusive study of nanoparticle formation [37].

1.3.1 FSP reactor characteristic

There are many importance components of FSP reactor including nozzle, syringe pump, 4 mass flow controllers, collector and glass fiber filter as shown in Figure 1.4. These components were described below.

1.3.1.1 Nozzle is composed of capillary tube with outer diameter of 0.91 mm and inner diameter of 0.6 mm. It stands on 1.22 mm base that was surrounded with annular gap with the highest area of 0.48 m^2. The precursor will be fed through the capillary tube while the dispersion gas (O_2) will come from annular gap with supporting flame from oxygen and methane gas. The capillary tube will be set over the cavity for stabilizing sprayed angle of precursor at any flow rates. Water is used to circulate the nozzle for cooling it.

1.3.1.2 Syringe pump is used for controlling the flow rate of the precursor to be higher than 3-6 cm^3/min. Syringe is made with teflon and/or stainless steel.

1.3.1.3 Mass flow controllers, there are 4 of them for controlling the flow rate of dispersion gas and supporting flame as the details below.

- The flow rate of supporting flame that is the mixture of oxygen and methane gas is in the range of 0-15 l/min.
- The flow rate for oxygen sheath gas is in the range of 0-15 l/min.
- The flow rate of oxygen dispersion gas should be in the range of 0-15 l/min. There are metering valve for adjusting the flow rate and mass flow controller for sending the data via data logger to the computer. This computer could save these data and draw the graph.

1.3.1.4 Collector is used for collecting the particles that originated through the flame. It is set over the nozzle for 38 cm. It can be used with glass fiber filter with the diameter of 25.7 cm. The circulated water is used for cooling this collector that is hollow inside from high temperature of flame. The top of collector is connected to the vacuum pump

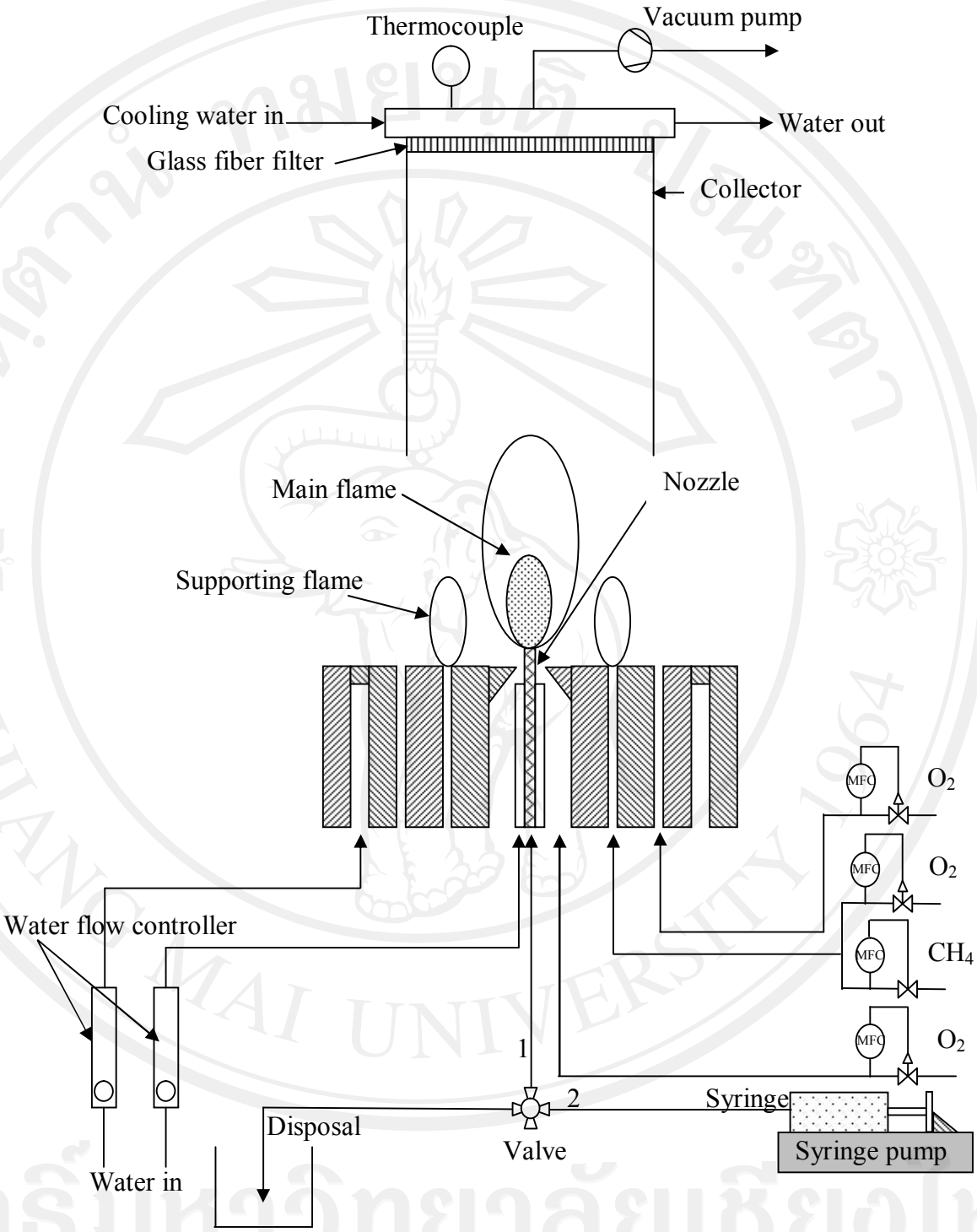

Figure 1.5 The schematic of experimental setup of FSP reactor

1.3.1.5 Glass fiber filter (Whatman GF/D, diameter of 25.7 cm) was connected to a vacuum pump for collecting the particles before they were released to the air. Both glass fiber and collector are in the fume hood.

1.4 Characterization techniques

1.4.1 X-ray diffraction method [38-41]

X-ray diffraction (XRD) is now a standard method for characterization of catalyst and generally has been employed to determine the crystalline phases, including solid solutions, and to measure the particles size and shape. It is also possible to follow *in situ* XRD changes that occur during activation and testing of catalysts.

Monochromatic X-ray, incident on a crystalline solid, is diffracted owing to the crystal structure of the solid. For a maximum to occur in the diffraction pattern at a particular angle of incidence θ (with respect to lattice planes (hkl), the Bragg equation must be followed

$$n\lambda = 2d_{hkl} \sin\theta_{hkl} \qquad (1.1)$$

where:

d_{hkl} = interplanar distance between (*hkl*) planes,

n = order of diffraction,

λ = wavelength of incident X-rays (e.g. 1.542 Å for copper K_α X-rays).

1.4.1.1 Identification of phases by XRD

XRD data is normally used for the phase identification, whereby the XRD pattern of a sample being examined can be compared with a Joint Committee Powder Diffraction Standards (JCPDS).

1.4.1.2 Particle size measurement by XRD [38-41]

For good quality crystalline material of dimension 0.1 nm is made up of approximately 1,000,000 crystal planes (assuming that d_{hkl} = 1 nm). When an X-ray collides with these planes close to the Bragg angle, diffraction intensity is not observed because the X-rays reflected from the multitude of parallel planes annihilate one another. With such materials diffraction peaks are produced only within a very narrow window very close to the Bragg angle. Particle sizes are often in the range of 1-100 nm for heterogeneous catalysts. In such circumstances the number of stacked planes per particle is in the range of 5-100. This results in the broadening of the XRD peaks because there are insufficient reflecting planes to annihilate phase reflection at angle that are fairly far removed from the Bragg angle.

This effect has been quantified as the Scherrer equation:

$$t_{hkl} = K\lambda / B_{hkl} \cos\theta_{hkl} \qquad (1.2)$$

where:

t_{hkl} is the particle size measured from X-rays diffracted from the (*hkl*) planes,

B is the peak width measured at half height measured in radius,

θ is the Bragg angle for the reflection, and

K is a constant which depends to some extent on the particles shape. For spherical particles K = 0.9.

Figure 1.6 demonstrates how particle size and shape can be determined by XRD analysis. A sample was analyzed by XRD and exhibited the pattern shown, namely one very narrow line and one rather broad one. In this case the apparent

conflict is caused by the shape of particle. X-rays reflected from the (100) planes 'see' a large particle and a narrow line results. X-rays reflected from the (001) planes 'see' a small particle and a broad line results.

When measuring particles size using XRD line broadening it is important to realize that the not all the broadening is due to the particle size effect. Near perfect crystals should produce extremely narrow XRD lines, but even here some broadening occurs because of instrumental factors. Instrumental contribution to line broadening is subtracted out by running the XRD of a good quality polycrystalline sample of the same materials.

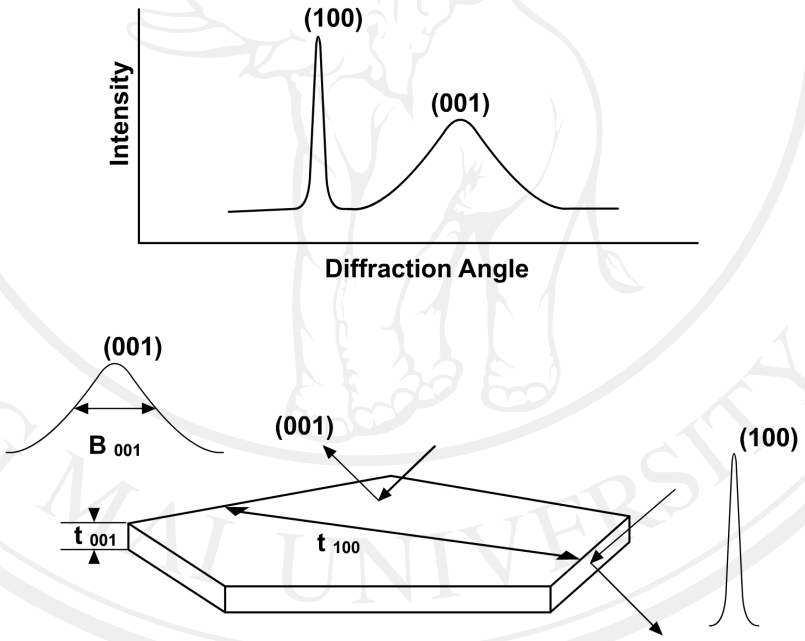

Figure 1.6 Schematic diagram of X-ray line broadening effects [39]

1.4.2 Surface area and porosity determination [38-41]

1.4.2.1 Surface area determination

Brunauer, Emmett and Teller developed the now famous BET equation for the determination of the surface area of a solid. The method is based on non-specific physisorption of a gas (N_2 or Ar) onto a solid close to the condensation temperature of

the adsorbing gas. Adsorption is characterized by an isotherm which represents the equilibrium amount of gas adsorbed on a solid at a given temperature as a function of pressure. Figure 1.7 is a typical isotherm for N_2 which forms the basis of the BET analysis. This figure shows formation of a near monolayer of adsorbate at low pressures, followed by multilayer formation which accelerates at high partial pressures. Hysteresis is observed also at p/p_0 above 0.8, namely differing behavior for whether the isotherm is determined by progressive addition or removal of adsorbate gas to the system.

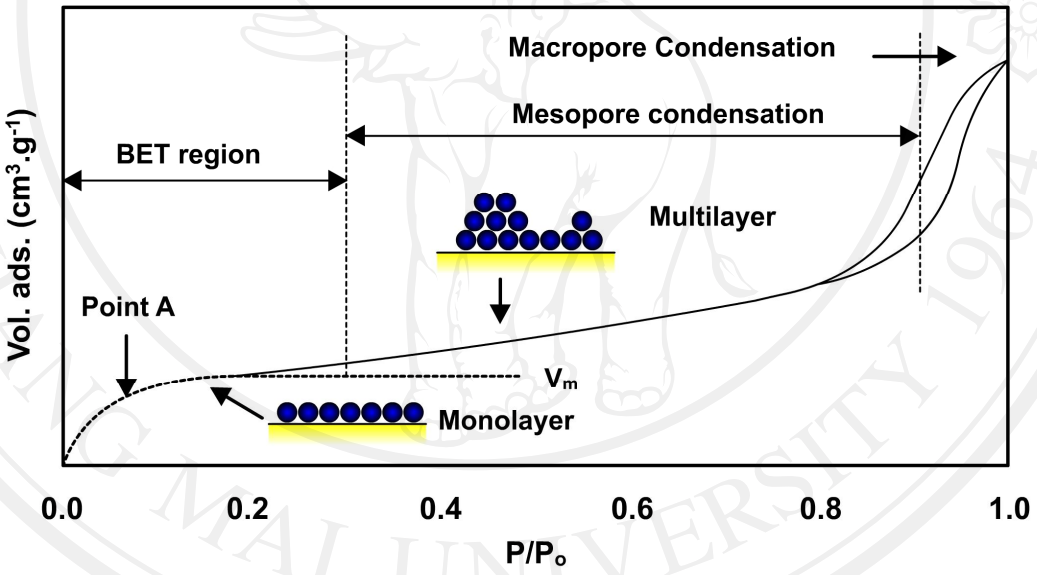

Figure 1.7 Typical isotherm for N_2 adsorption-desorption on γ-Al_2O_3 [39]

Point A in Figure 1.7 corresponds to the stage at which there is approximately monolayer coverage. There is a difficulty in determining this point exactly as multilayer physisorption which can occur before monolayer coverage is complete. BET equation is as follow:

$$\frac{p}{V(p_0 - p)} = \frac{1}{V_m C} + \frac{(C-1)p}{CV_m p_0} \qquad (1.3)$$

where:

V is the volume, reduced to standard conditions (STP) of gas adsorbed per unit mass of adsorbent at a given pressure, p and constant temperature,

p_0 is the saturation pressure at the measurement temperature,

V_m is the volume of gas adsorbed at STP per unit mass of adsorbent, when the surface is covered by a unimolecule layer of adsorbate, and

C is a constant, related to the free energy of adsorption.

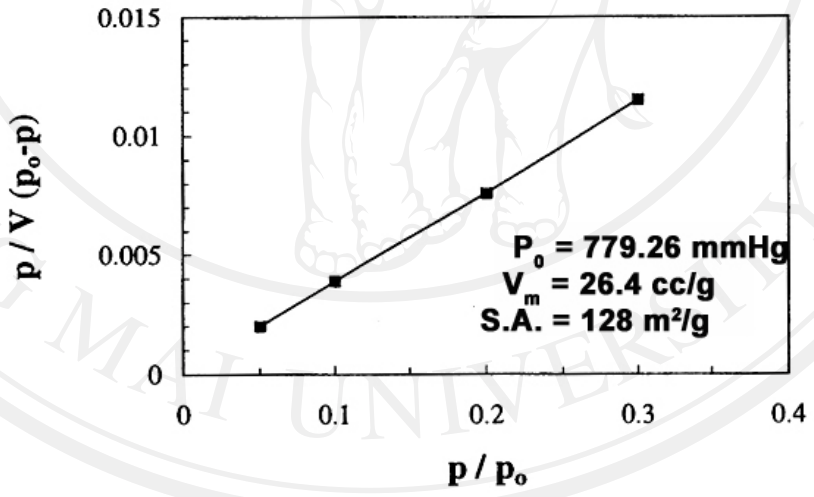

Figure 1.8 BET plot for surface area (S.A.) determination for γ-Al_2O_3 [39]

According to equation 1.3 a plot of $p/V(p_0-p)$ versus p/p_0 should yield a straight line. The surface area is then calculated using:

$$S_{\mathrm{BET}} = \frac{V_{\mathrm{m}} A_{\mathrm{m}} N_{\mathrm{a}}}{V_{\mathrm{mol}}} \qquad (1.4)$$

where:

N_a is Avogadro's number (6.02×10^{23}),

V_{mol} is the molar volume of absorbate gas at STP (22.4 mol^{-1}),

A_m is the cross-sectional area of absorbed gas ($A_m(N_2)$ = 0.162 nm^2).

When nitrogen is the adsorbing gas this reduces to:

$$S_{BET} = 4.353 V_m \qquad (1.5)$$

The BET equation is applicable within the range of relative pressures $0.05 < p/p_0 < 0.3$. At higher relative pressures, the BET equation is usually inaccurate owing to the effects of capillary condensation in the smallest micropores. Figure 1.8 shows analysis of the data from Figure 1.6 in the range $0 < p/p_0 < 0.3$. The surface area in this case was 128 m^2/g.

1.4.2.2 Pore size distribution [39]

The International Union of Pure and Applied Chemistry (IUPAC) has classified pores into several size ranges. Pores with diameters less than 2 nm are termed micropores, pores with a diameter greater then 2 nm but less than 50 nm are termed 'transitional' or mesopores, while pores with diameters greater than 50 nm are terms macropores. In addition to the determination of the surface area of porous solids it is essential that the pore shape and pore size distributions are know to describe completely the textural properties of porous solids.

Traditionally pores with diameters less than 50 nm have been determined by nitrogen adsorption-desorption isotherms, while pores diameters greater than 100 nm have been measured with mercury porosimeters.

Two separate approaches are required to determine micropore and mesopore size distributions. For micropores devised a method for the determination of micropore area distribution and micropore volume distributions (the MP method) by manipulation of isotherm adsorption data Figure 1.9. It is essentially a modification of Lippens and de Boer's, *t*-method where the variation of the thickness (*t*) of adsorbed N_2 layers with relative pressure (p / p_0) on a porous solid is compared with a standard *t*-curve from a non-porous solid. The thickness of the adsorbed N_2 layers is obtained by dividing the liquid volume of N_2 adsorbed by BET surface area:

$$t = \frac{V_{\text{liq}}}{S_{\text{BET}}} \times 10^3 \text{ (nm)} \qquad (1.6)$$

At higher relative pressures (higher values of t) deviations from a straight line due to micropore capillary condensation are used to evaluate micropore shape, size and volume distributions.

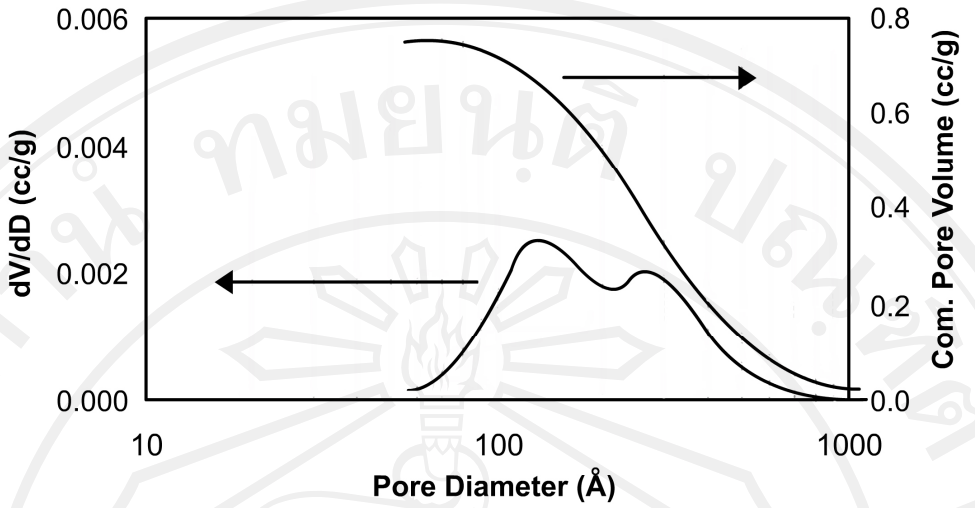

Figure 1.9 BJH analysis of data from Figure 1.8 showing differential and cumulative mesopore volume distributions for γ-Al_2O_3 [39]

Information on mesopores comes from the isotherm at p/p_0 values above 0.25. The isotherm in Figure 1.7 shows a splitting into an adsorption and a desorption branch. This hysteresis contains valuable information on mesopore geometry and the phenomenon is governed by the Kelvin equation. The Kelvin equation with N_2 as the adsorbate is:

$$r_k = \frac{0.415}{\log(p_0 / p)} \tag{1.7}$$

The Kelvin radius (r_k) indicates that radius into which condensation occurs at the required relative pressure. The actual pore radius is given by:

$$r_p = r_k + t \tag{1.8}$$

The term *t* refers to thickness of a multilayer of adsorbed N_2 existing on the pore wall when evaporation or condensation occurs which is of the same depth as the adsorbed N_2 layer on a non porous surface.

$$t = 3.54\left[\frac{5}{2.303\log(p/p_0)}\right]^{1/2} \quad (1.9)$$

Numerical integration methods such as the BJH method can be used to evaluate mesopore area and volume distribution utilizing the Halsey equation. Figure 1.9 presents a BJH treatment of the isotherm shown in Figure 1.7, in terms of cumulative mesopore volume and size distribution.

1.4.3 Transmission electron microscopy and diffraction [38-40, 42]

Electron microscopy (EM) provides local structure information on the samples in both real and reciprocal space, for example local structural information about the surface and the bulk of the sample at the atomic level, together with chemical, electronic and three-dimensional structural information are now routinely available. Electron-sample interactions and scattering are fundamental to EM. EM is a diffraction technique in which crystals diffract electrons in accordance with Bragg's law, $n\lambda = 2d\sin\theta$, where λ is the wavelength of the electrons, *d* is the lattice planar spacing of the *hkl* reflection and θ is the scattering angle. Discovery of the electron and the particles and wave duality of electrons has been well documented in the literature. The electron has a low mass and is negatively charged. It can be easily deflected when close to electron and the positive nucleus of the sample atom. These interactions are termed Coulombic or electrostatic interactions and lead to electron

scattering. Electron microscopy deals with a complex electron wave with both its amplitude and phase modulated, as the electrons interact with matter. This interaction generates elastic scattering and a variety of other signals which can be used to obtain structural and chemical information about a sample as shown in Figure 1.10(a). Elastic scattering occurs when incident electrons interact with the potential field formed by the nuclei of matter involved with essentially no energy loss in momentum transfer, whilst inelastic scattering occurs when interactions between incident electrons and the electrons of matter occur and scattered electrons lose energy.

Transmission electron microscope (TEM), electrons are transmitted through the sample. Normally the incident and scattered electrons are referred to as electron beams. In TEM, the electron beam is transmitted through the instrument's optics. The TEM has an electron gun and electromagnetic lenses which include condenser and objective lenses. The condenser lenses converge and control the electron beam and illuminate the sample, and the objective lenses forms the image of the sample and diffraction. The images and diffractions are then magnified by other lenses in the system. A base reference line passing through the centre of all the lenses is called the optic axis of the electron microscope.

Figure 1.10(b) shows a 'ray diagram' for a finite object which scatters radiation and can be used to understand the image formation in an electron microscope. Rays scattered at an angle θ are gathered by the objective lens and converged to a point in the image plane. Parallel rays are focused in the back focal plane (bfp) of the lens. The intensity distribution in the bfp gives rise to diffraction. The diffraction pattern formed may be regarded as the Fourier Transform (FT) of the crystal. An apertured inverse Fourier transforms (FT) in the objective lens forms the

image. The objective lens takes the electrons emerging from the exit surface of the sample and disperses them to create an electron diffraction pattern (DP) in the bfp and recombines them to form an image in the image plan. In a TEM, accelerating electron voltages are normally between 100-400 keV and lower (a few hundred electron volts to ~30 keV) for scanning EM (SEM). Principles of EM imaging and diffraction are shown in Figure 1.10(c). In EM, a two-dimensional planar projection of a three-dimensional object is observed.

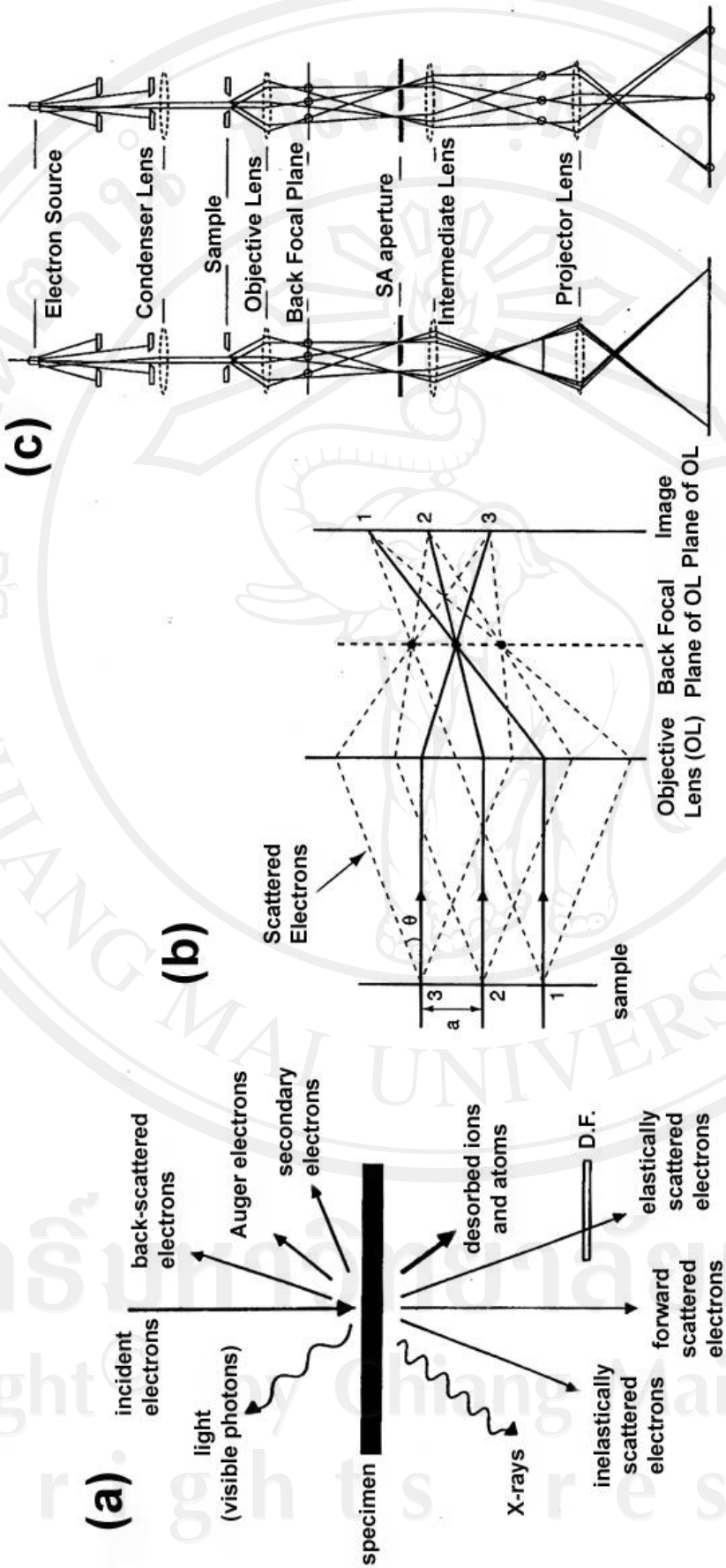

Figure 1.10 (a) Signals generated during electron beam-sample interactions; (b) a 'ray diagram' of image formation; and (c) a schematic diagram of the principles of electron microscopy: (A) imaging and (B) diffraction [38].

1.4.4 Chemical composition analysis [38-40, 42]

Analytical EM using electron-stimulated characteristic X-rays is a well-known chemical composition characterization technique for analyzing materials. High spatial resolution chemical analyses (from areas of a few nm or less) using electron nanoprobes are now possible in a modern EM and can provide information of the catalyst composition at the subnanometer level. Details of EDX in the EM are described and some important definitions are highlighted in the following sections.

1.4.4.1 X-ray spectroscopy in the electron microscope [42]

In electron-sample interactions, X-rays can be formed during inelastic scattering of electrons. The following principles describe the generation and character of the X-rays.

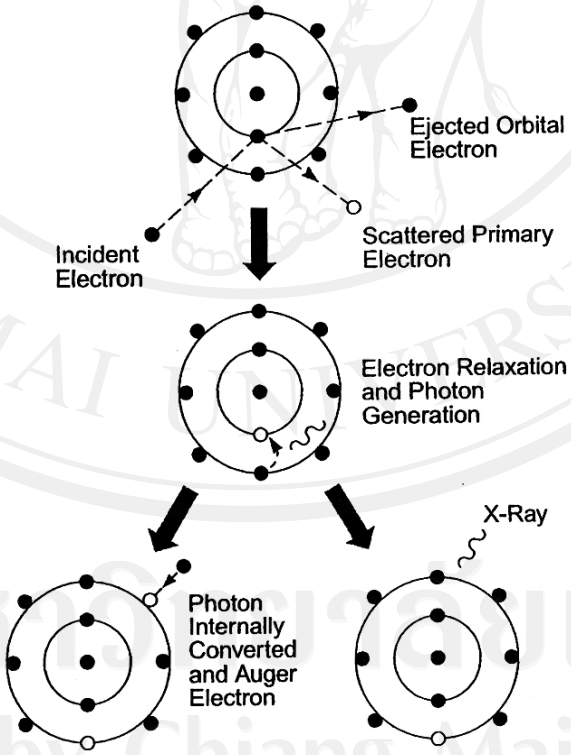

Figure 1.11 The process of electron-stimulated X-ray emission in the electron microscope [38]

Characteristic of X-ray spectroscopy is described as the interaction between a high-energy electron forms the beam and an inner-shell electron from the sample atom results in the ejection of a bound inner-shell electron from the attractive field of the nucleus in the sample atom, leaving the atom in an excited state with an electron shell vacancy. Deexcitation by transition from the outer shell involves a change in the energy state of the atom between sharply defined levels, producing X-rays (or Auger electrons). The process is elucidated in Figure 1.11. These X-rays are characteristic of the elements in the sample and are used for composition analysis. EDX, in which X-ray intensities are measured as a function of the X-ray energy, is the most convenient and common method for chemical composition analysis in the electron microscope

Continuum is described as the deceleration of beam electrons (i.e. those which do not participate in removing sample electrons) leads to the production of a continuous range of X-rays. They contribute to the background of a spectrum and are termed Bremmsstrahlung X-rays.

Chemical composition analysis complementing the microstructural information obtained from EM is known as analytical EM (AEM). Important compositional variations or non-stoichiometry in a material which is seemingly 'phase pure or stoichiometric' by the criterion of bulk diffraction techniques and compositions of surface layers can be revealed using AEM. For quantitative microanalysis a ratio method for thin crystals is used, given by the equation:

$$C_A / C_B = K_{AB} I_A / I_B \qquad (1.10)$$

where C_A and C_B are the concentrations of elements A and B and I_A and I_B are the background subtracted peak intensities for A and B; and typically a few dozen crystals are analyzed. The sensitivity factor K_{AB} is determined using appropriate standards. For bulk materials, more complex correction procedures are required for atomic number (Z), absorption (A) and X-ray fluorescence (F). Thus, AEM provides real space imaging together with crystallographic and microcompositional information about the sample on the very fine scale. Furthermore, AEM can be used to obtain partial occupancies within cation sites, (and under special conditions, in anion sites). When elemental peaks overlap, wavelength dispersive X-ray spectroscopy (WDS - where X-ray intensities are measured as a function of wavelength) may be advantageous for composition analysis. Detection sensitivity in WDS can be very high (<100 ppm), due to the much higher X-ray count rates.

1.4.4.2 Selected-area diffraction [42]

The technique relies upon the fact that the electron beam after diffraction by the specimen forms a miniature diffraction pattern (ring or spots) in the back focus plane of the objective lens (Figure 1.12(a)). Electron diffracted in the same directions OA, O′A′ come together to form a spot P in the back focal plane of the lens. Similarly the diffraction spot Q is formed by electron diffracted at an equal angle on the opposite side of the undeviated beam. If the first projector lens (or the diffraction lens in a four-lens imaging system) is now weakened so that it is focused in this plane instead of the image plane of the objective lens (i.e. the first intermediate image plane), the pattern is projected and enlarged on to the screen of the microscope. If the lens currents for this mode of imaging are preset the microscope can be switched

alternately between imaging the specimen and projecting its diffraction pattern (Figure 1.12(b)).

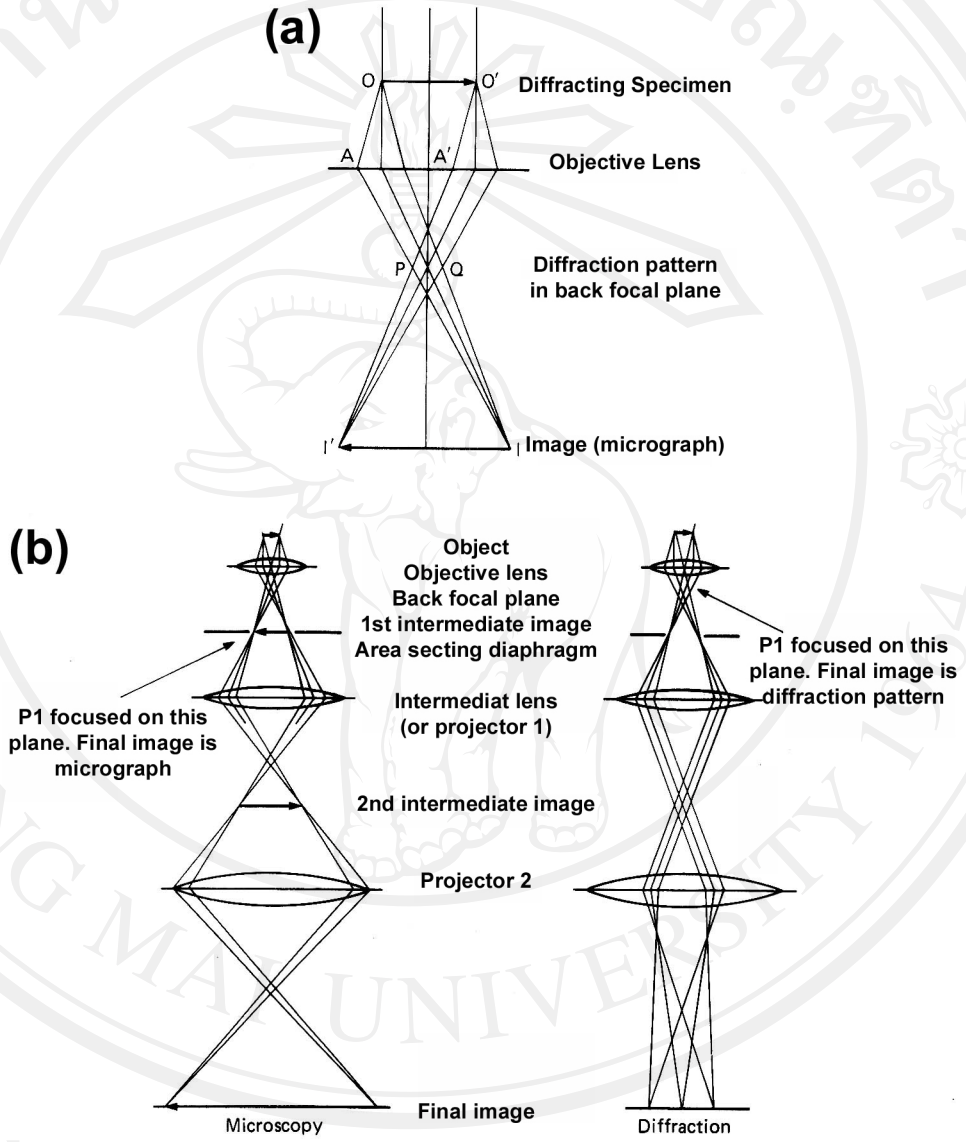

Figure 1.12 (a) Ray diagram showing the formation of the diffraction pattern and intermidate image by the objective lens (b) In a three-lens microscope the intermediate lens (or projector 1) is normally focused on the intermediate image formed by objective lens [42].

When P1 is weakened to focus on the back focal plane of the objective lens the final image is an enlarged diffraction patterns. The selected area diaphragm ensures that only electrons coming from a chosen region in the specimen contribute to the diffraction pattern. Moreover, if a diaphragm containing an aperture of diameter D is inserted into the plane of the first intermediate image, it will pass only those electrons coming from a part of the object of diameter D/M, where M is the magnification of the objective lens. With this area-selecting aperture in place, switching to the diffraction mode results in a diffraction pattern being formed only by those electrons originating from the chosen small area of object.

1.4.4.3 Measurements of electron diffraction patterns [42]

The electron diffraction camera or its equivalent, diffraction stage of the TEM, the relationship $\lambda L=Rd$ can be obtained for the precise determinations of lattice spacing once L has been measured and λ calculated. If the gun voltage is not known accurately it is better to determine the product λL (camera constant) experimentally by calibrating with a stand substance such as thallium chloride or aluminum. Lattice spacing may be measured to 1% by very careful working, but 5% is a more practical aim which may still be sufficiently precise to enable materials to be identified by electron diffraction, using the crystallographic data provided by Joint Committee Powder Diffraction Standards (JCPDS) powder diffraction file. Selected area diffraction can also be very useful for the purely qualitative assessment of the degree of crystallinity of a specimen.

1.4.5 Scanning Electron Microscope (SEM) [43]

Scanning electron microscope, the surface of a solid sample is scanned in a raster pattern with a beam of energetic electrons. Several types of signals are

produced from a surface in this process, including backscattered, secondary, and Auger electrons; X-ray fluorescence photons; and other photons of various energies. All of these signals have been used for surface studies, but the two most common are 1) backscattered and secondary electrons, which serve as the basis of scanning electron microscopy, and 2) X-ray emission, which is used in electron microprobe analysis.

1.4.5.1 Instrumentation

Figure 1.13 is a schematic of a combined instrument that is both a scanning electron microscope and a scanning electron microprobe. The common electron gun source and electron focusing system are used but that the electron microscope employs an electron detector, whereas the microprobe uses an X-ray detector. The magnetic condenser and objective lens system shown in Figure 1.13 serve to reduce the image to a final spot size on the sample of 5 to 200 nm. The condenser lens system, which may consist of one or more lenses, is responsible for the through put of the electron beam reaching the objective lens; the objective lens is responsible for the size of the electron beam impinging on the surface of the sample. Typically, an individual lens is cylindrically symmetrical and between 10 and 15 cm in height. Scanning with a SEM is accomplished by the two pairs of electromagnetic coils located within the objective lens (see Figure 1.13); one pair deflects the beam in the x direction across the sample, and the other pair deflects it in the y direction. Scanning is controlled by applying an electrical signal to one pair of scan coils, such that the electron beam strikes the sample to one side of the center axis of the lens system. By varying the electrical signal to this pair of coils as a function of time, the electron beam is moved in a straight line across the sample and then returned to its original position. After completion of the line scan, the other set of coils is used to deflect the

beam slightly, and the deflection of the beam using the coils is repeated. Thus, by rapidly moving the beam, the entire sample surface can be irradiated with the electron beam. The signals to the scan coils can be either analog or digital. Digital scanning has the advantage that it offers very reproducible movement and location of the electron beam. The signal from the sample can be encoded and stored in digital form along with digital representations of the x and y positions of the beam. The signals that are used to drive the electron beam in the x and y directions are also used to drive the horizontal and vertical scans of a cathode-ray tube (CRT). The image of the sample is produced by using the output of a detector to control the intensity of the spot on the CRT. This method of scanning produced a map of the sample in which there is a one-to-one correlation between the signal produced at a particular location on the sample surface and a corresponding point on the CRT display. The magnification (M) achievable in the SEM image is given by

$$M=W/w \tag{1.11}$$

where W is the width of the CRT display and w is the width of a single line scan across the sample. Because W is a constant, increased magnification is achieved by decreasing w. The inverse relationship between magnification and the width of the scan across the sample implies that a beam of electrons that has been focused to an in finely small point could provide infinite magnification. A variety of other factors, however, limit the magnification that is achievable to a range from about $10\times$ to $100,000\times$.

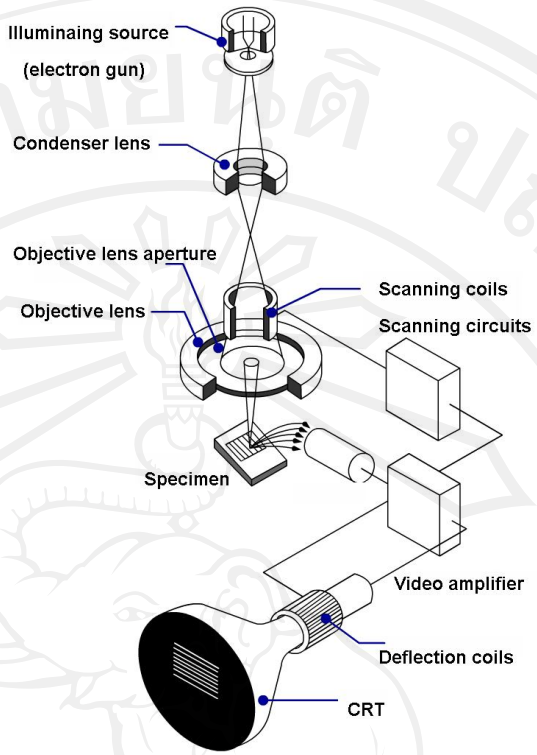

Figure 1.13 Schematic diagram of scanning electron microscope with CRT display [43]

1.4.5.2 Interaction of electron beams with solids

The versatility of the scanning electron microscope and microprobe for the study of solids arises from the wide variety of signals that are generated when the electron beam interacts with the solid. The signals are included: backscattered electrons, secondary electrons, and X-ray emission. The interactions of a solid with an electron beam can be divided into two categories: elastic interactions, which affect the trajectories of the electrons in the beam without altering their energies significantly, and inelastic interactions, which result in transfer of part or all of the energy of the electrons to the solid. The excited solid then emits secondary electrons, Auger electrons, X-rays, and sometimes longer wavelength photons.

- **Elastic scattering**

When an electron collides elastically with an atom, the direction of the electron changes, but the speed of the electron is virtually unaffected, so that the kinetic energy of the electron remains essentially constant. The angles of deflection for any given collision are random and vary from 0 to 180 deg. Some of the electrons eventually lose energy by inelastic collisions and remain in the solid; the majority, however, undergoes numerous collisions and as a result eventually exits from the surface as backscattered electrons. It is important to note that the beam of backscattered electrons has a much large diameter than the incident beam- that is, for a 5-nm incident beam; the backscattered beam may have a diameter of several micrometers. The diameter of the backscattered beam is one of the factors limiting the resolution of an electron microscope.

- **Secondary electron production**

The surface of a solid is bombarded with an electron beam having an energy of several keV that electrons having energies of 50 keV or less are emitted from the surface along with the backscattered electrons. The number of these secondary electrons is generally one half to one fifth or less of the number of backscattered electrons. Secondary electrons are produced as a result of interactions between the energetic beam electrons and weakly bound conduction electrons in the solid, which leads to ejection of the conduction band electrons with a few electron volts of energy. Secondary electrons are produced from a depth of only 50 to 500 Å and exit in a beam that is slightly larger in diameter than the incident beam.

- X-ray emission

A third product of electron bombardment of a solid is X-ray photons. Both characteristic line spectra and an X-ray continuum are produced and emitted from the surface of the sample. This radiation serves as a basis for the electron microprobe.

1.4.6 UV-Vis absorption spectroscopy [44]

In transmission spectroscopy, where a beam of light is passed through a sample, the transmittance is the ratio of intensities of transmitted to incident light:

$$T = \frac{I}{I_0} \tag{1.12}$$

where T is the transmittance (1 for a completely transparent sample), I is the intensity of transmittance light, I_0 is the intensity of the incident beam. In an analogous fashion, the remittance of a diffusely reflecting sample is the ratio of intensities of reflected to incident light:

$$R_\infty = \frac{J}{I_0} \tag{1.13}$$

where R_∞ is the absolute remittance, J is the intensity of the reflected radiation, and I_0 is again the intensity of the incident beam. The ∞ subscript denotes that the sample is "infinitely thick"; in other word, none of the light irradiating the sample penetrates to the bottom of the sample holder. This is usually the case when the sample thickness is

approximately 5 mm or more. A perfect diffusely reflecting substance, practically never attained, would have $R_\infty = 1$.

Since it is not practical to measure R_∞, the absorbed remittance, the measured quantity is usually the relative remittance, R'_∞:

$$R'_\infty = \frac{R_{\infty\text{sample}}}{R_{\infty\text{standard}}} \tag{1.14}$$

Notice that if $R_{\infty\text{standard}}$=1, then the absolute and relative remittances must be equal.

The relative remittance is analogous to transmittance in transmission spectroscopy. Transmission spectroscopy is often conveniently present data in absorbance in linear fashion which related to the concentration of absorbing species. In an analogous fashion, it is possible to plot log ($1/R'_\infty$) against wavelength or frequency. This is so called apparent absorbance units. This does not imply, however, that Beer's law is valid for diffuse reflectance spectroscopy.

Ideally one would like a function, like Beer's law in transmission spectroscopy, to linearly relate analyst concentration with the reflectance characteristics of a diffusely reflecting sample. The function often use is that derived by Kubelka-Munk:

$$F(R_\infty) = \frac{(1-R_\infty)^2}{2R_\infty} = \frac{K}{S} = \frac{2.303\varepsilon C}{S} \tag{1.15}$$

where K is the absorption coefficient (twice the Beer's law absorption coefficient), S is twice the scattering coefficient of the sample, ε is the absorptivity, and C is the analyst concentration.

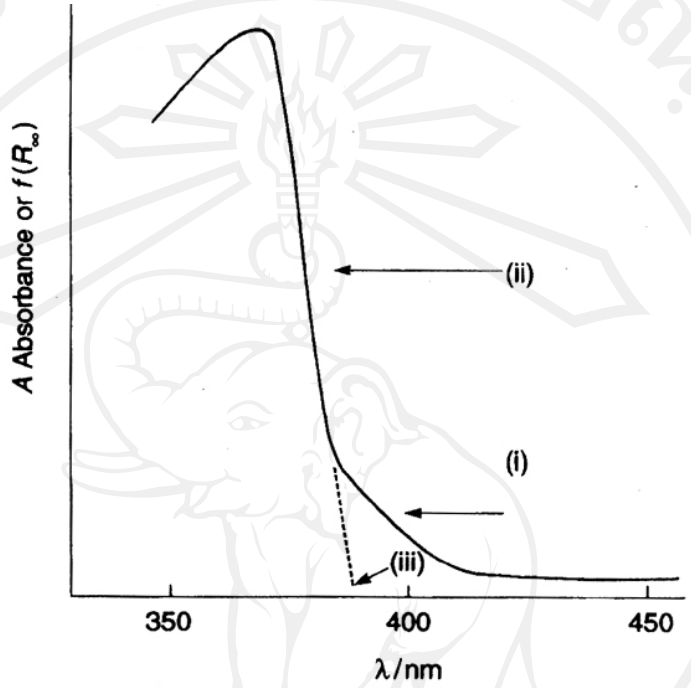

Figure 1.14 Diffuse reflectance spectrum of the fundamental absorption edge of titanium dioxide powder. Absorbance ($(F(R_\infty))$ vs. wavelength: (i) indirect transition; (ii) direct transition; (iii) direct band gap; $E_g = hc/\lambda_g$ [44]

The interaction of near-UV photons with a typical photocatalytic material (e.g., finely divided ZnO powder) is illustrated in Figure 1.14. The shape of the absorption edge reveals to some extent the shapes of the densities of electronic states in the valence band and in the adjacent conduction band and a diagrammatic representation of this situation is illustrated in Figure 1.15(a). The onset of the absorption edge (lowest energy) indicates the minimum energy required to effect the excitation of an electron from the highest occupied energy state of the valence band

into the lowest available energy state of the conduction band. This transition may not necessarily involve the coupling of the electric vector of the photon directly. The wave functions of the two state involved in the cases where this occurring, this process is termed a direct transition and results in a small change ($\Delta\tilde{k} \approx 0$) in the wave vector of the electron involved following its excitation to the conduction band. More frequently, the magnitude of the wave vector ($\tilde{k}'_{cb}$) of the lowest energy state in the conduction band does not correspond to that of the electron at the highest energy of the valence band ($\tilde{k}_{vb}$), and as a consequence of the significant difference in these wave vector ($\Delta\tilde{k}$) requires that the excitation of the electron from the lower state (valence band (VB)) to the highest state (conduction band (CB)) is accompanied by the participation, simultaneously, of an elastic wave within the lattice of the solid (illustrated in Figure 1.15 (b)).

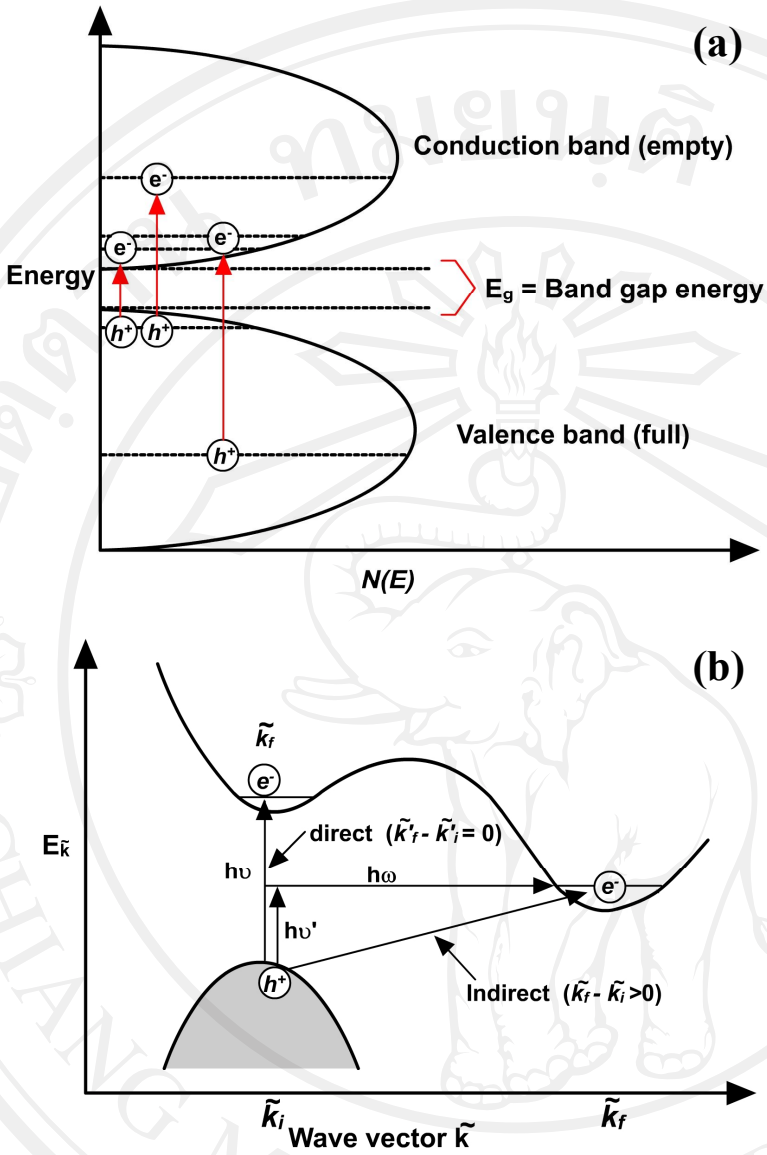

Figure 1.15 (a) Schematic energy band diagram showing hole-electron pair formation as a consequence of differing energies of incident radiation; (b) schematic energy band diagram (energy vs. wave vector $\tilde{k}$) illustrating the difference between direct and indirect transitions [44]

In such circumstances, the transition probabilities of the two processes differ significantly in magnitude, a useful analog being with two-body (direct) and three described, the 'bodies' are the photon and the electrons in the direct transition or the photon, the phonon and the electron in the indirect transition.

At photon energies higher in magnitude than the minimum required value effect the transitions of the types described. Electrons from the highest occupied states in the valence band can be promoted to a higher energy states within the conduction band or into other unoccupied bands that may exist at even larger energies. In general, the range of energies (ΔE) of the conduction band from its lowest value to the highest will be greater than the corresponding range of energies of the valence band. The onset of absorption may be due to an indirect process with a correspondingly smaller value of $-\mathrm{d}A/\mathrm{d}\lambda$. Direct processes with larger $-\mathrm{d}A/\mathrm{d}\lambda$ values will be likely at higher photon energies. Additionally the adsorption of higher-energy photons may raise electrons from lower-energy states in the valence band to the lower regions of the conduction band. However, the accompanying hole state in the valence band will have a larger momentum than one created nearer to the top of the band.

1.4.7 Photoluminescence (PL) [45-46]

Photoluminescence (PL) is the spontaneous emission of light from a material under optical excitation. The excitation energy and intensity are chosen to probe different regions and excitation concentrations in the sample. PL investigations can be used to characterize a variety of material parameters. PL spectroscopy provides electrical (as opposed to mechanical) characterization, and it is a selective and extremely sensitive probe of discrete electronic states. Features of the emission spectrum can be used to identify surface, interface, and impurity levels and to gauge alloy disorder and interface roughness.

When light of sufficient energy is incident on a material, photons are absorbed and electronic excitations are created. Eventually, these excitations relax and the

electrons return to the ground state. If radiative relaxation occurs, the emitted light is called PL. This light can be collected and analyzed to yield a wealth of information about the photoexcited material. The PL spectrum provides the transition energies, which can be used to determine electronic energy levels. The PL intensity gives a measure of the relative rates of radiative and nonradiative recombination. Variation of the PL intensity with external parameters like temperature and applied voltage can be used to characterize further the underlying electronic states and bands.

PL is simple, versatile, and nondestructive. The instrumentation that is required for ordinary PL work is modest: an optical source and an optical power meter or spectrophotometer. A typical PL set-up is shown in Figure 1.16. Because the measurement does not rely on electrical excitation or detection, sample preparation is minimal. This feature makes PL particularly attractive for material systems having poor conductivity or undeveloped contact/junction technology. Measuring the continuous wave PL intensity and spectrum is quick and straightforward. On the other hand, investigating transient PL is more challenging, especially if recombination processes are fast. Instrumentation for time-resolved detection, such as single photon counting, can be expensive and complex. Even so, PL is one of the only techniques available for studying fast transient behavior in materials.

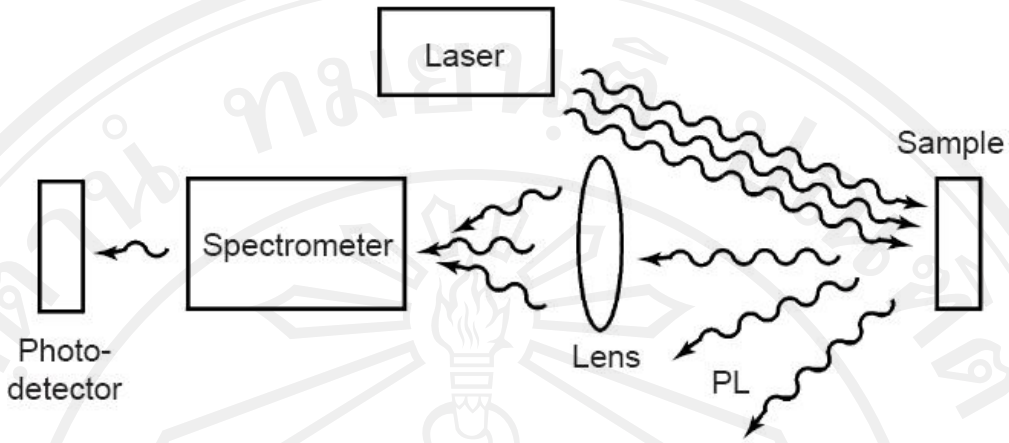

Figure 1.16 Typical experimental set-up for photoluminescence measurement [45]

In the bulk of a crystalline material, translational symmetry leads to the formation of electronic energy bands. Defects and impurities break the periodicity of the lattice and perturb the band structure locally. The perturbation usually can be characterized by a discrete energy level that lies within the bandgap. Depending on the defect or impurity, the state acts as a donor or acceptor of excess electrons in the crystal. Electrons or holes are attracted to the excess or deficiency of local charge due to the impurity nucleus or defect, and Coulomb binding occurs. The situation can be modeled as a hydrogenic system where the binding energy is reduced by the dielectric constant of the material. Because electrons and holes have different effective masses, donors and acceptors have different binding energies. When the temperature is sufficiently low, carriers will be trapped at these states. If these carriers recombine radiatively, the energy of the emitted light can be analyzed to determine the energy of the defect or impurity level. Shallow levels, which lie near the conduction or valence band edge, are more likely to participate in radiative recombination, but the sample temperature must be small enough to discourage thermal activation of carriers out of

the traps. Deep levels tend to facilitate nonradiative recombination by providing a stop-over for electrons making their way between the conduction and valence bands by emitting phonons. Several intrinsic and impurity transitions are illustrated in Figure 1.17.

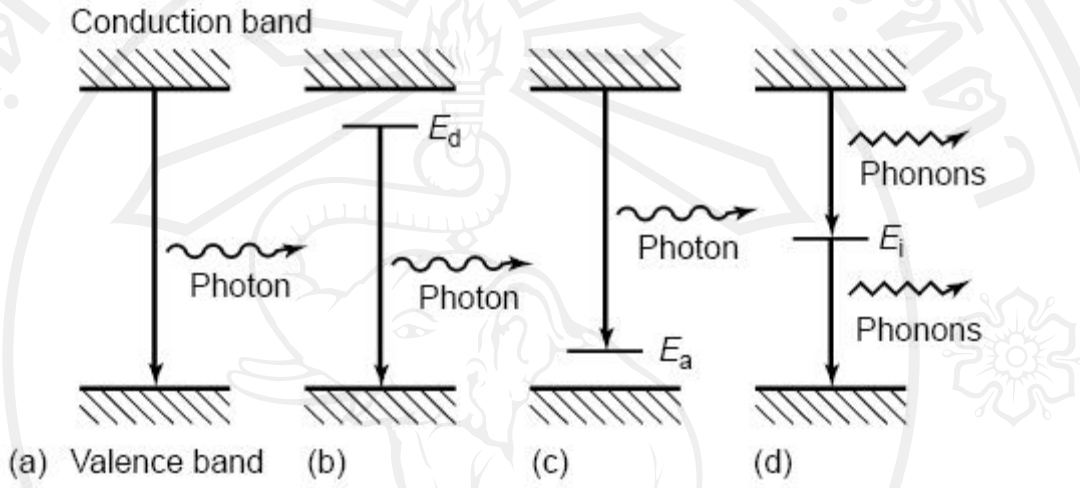

Figure 1.17 (a–c) Radiative recombination paths: (a) band-toband; (b) donor to valence band; (c) conduction band to acceptor. (d) Nonradiative recombination via an intermediate state [45].

REFERENCES

1. Liqiang J., Dejun W., Baiqi W., Shudan L., Baifu X., Honggang X., Jiazhong S. Effects of noble metal modification on surface oxygen composition, charge separation and photocatalytic activity of ZnO nanoparticles, *J. Mol. Catal., A- Chem.*, 2006, **244**, 193-200.
2. Wang H., Xie C., Zhang W., Cai S., Yang Z., Gui Y. Comparison of dye degradation efficiency using ZnO powders with various size scales, *J. Hazard. Mater.*, 2007, **141**, 645-652.
3. Beek W.J.E., Wienk M.M., Kemerink M., Yang X., Janssen R.A.J. Hybrid zinc oxide conjugated polymer bulk heterojunction solar cells, *J. Phys. Chem. B*, 2005, **109**, 9505-9516.
4. Beek W.J.E., Wienk M.M., Janssen R.A.J. Efficient hybrid solar cells from zinc oxide nanoparticles and a conjugated polymer, *Adv. Mater.*, 2004, **16**, 1009-1013.
5. Cheng X.L., Zhao H., Huo L.H., Gao S., Zhao J.G. ZnO nanoparticulate thin film: preparation, characterization and gas-sensing property, *Senser Actuat. B-Chem.*, 2004, **102**, 248-252.
6. Comini E., Faglia G., Ferroni M., Sberveglieri G. Gas sensing properties of zinc oxide nanostructures prepared by thermal evaporation, *Appl. Phys. A-Mater*, 2007, **88**, 45–48.
7. Özgür Ü., Alivov Y.I., Liu C., Teke A., Reshchikov M.A., Doğan, S., Avrutin V., Cho S.J., Morkoç H. A comprehensive review of ZnO materials and devices, *J. Appl. Phys.*, 2005, **98**, 041301(1)-041301(103).

8. Wang Z.L. Zinc oxide nanostructures: growth, properties and applications, *J. Phys.-Condens. Mat.*, 2004, **16**, 892-858.

9. Norton D.P., Heo Y.W., Ivill M.P., Ip H., Pearton, S.J., Chisholm M.F., Steiner T. ZnO: growth doping & processing, *Materialstoday*, 2004, **2**, 34-40.

10. Sakthivel S., Geissen S.U., Bahnemann D.W., Murugesan V., Vogelpohl A., Enhancement of photocatalytic activity by semiconductor heterojunctions:α-Fe_2O_3, WO_3 and CdS deposited on ZnO, *J. Photoch. Photobio. A*, 2002, **148**, 283-293.

11. Rodriguez-Paez J.E., Canallero A.C., Villegas M., Moure C., Duran P., Fernanolez J.F. Controlled precipitation methods: formation mechanism of ZnO nanoparticles condensation technique, *J. Eur. Ceram. Soc.*, 2001, **21**, 925-930.

12. Mondelaers D., Vanhoyland G., Van-den R.H., Haen, J.D., Van M.K., Mullens J., Van-Poucke L. C. Synthesis of ZnO nanopowders via an aqueous acetate-citrate gelation method, *Mater. Res. Bull.*, 2002, **37**, 901-914.

13. Kwon Y.J., Kim K.H., Lim C.S., Shim K.B., Characterization of ZnO nanopowders synthesized by the polymerized complex method via an organochemical route, *J. Ceram. Process Res.*, 2002, **3**, 146-149.

14. Zhang S.C., Li X.G. Preparation of ZnO particles by Precipitation transformation method and its inherent formation mechanisms, *Colloid Surface A.*, 2003, **226**, 35-44.

15. Tani T., Mädler L., Pratsinis S.E. Homogeneous ZnO nanoparticles by flame spray pyrolysis, *J. Nanopart. Res.*, 2002, **4**, 337-343.

16. Pratsinis S.E. Flame aerosol synthesis of ceramic powders, *Prog. Energ. Combust. Sci.*, 1998, **24**, 197-219.

17. Mädler L., Kammler H.K., Mueller R., Pratsinis S.E. Controlled synthesis of nanostructured particles by flame spray pyrolysis, *J. Aerosol Sci.* 2002, **33**, 369-389.

18. Müller R., Mädler L., Pratsinis S.E. Nanoparticle synthesis at high production rates by flame spray pyrolysis, *Chem. Eng. Sci.* 2003, **58**, 1969-1976.

19. Tilley R.J.D. The crystal chemistry of the higher tungsten oxides, *Int. J. Refract. Met. H.*, 1995, **13**, 93-109.

20. Granqvist C.G. Electrochromic tungsten oxide films: review of progress 1993-1998, *Sol. Energ. Mat. Sol. C.*, 2000, **60**, 201-262.

21. Deb S. K. Opportunities and challenges in science and technology of WO_3 for electrochromic and related applications, *Sol. Energ. Mat. Sol. C.*, 2008, **92**, 245-258.

22. Hoel, A. "Electrical Properties of Nanocrystalline WO_3 for Gas Sensing Applications" Comprehensive Summaries of Uppsala Dissertations from the Faculty of Science and Technology, Uppsala University, Sweden, 2004.

23. Aird A. Domeneghetti M.C., Mazzi F., Tazzoli V., Salje, E.K.H. Sheet superconductivity in WO_{3-x}: crystal structure of the tetragonal matrix, *J. Phy-Condens. Mat.*, 1998, **10**, L569-L574.

24. Anders S., Anders A., Rubin M., Wang Z., Raoux S., Kong F., Brown I.G. Formation of metal oxides by cathodic arc deposition, *Surf. Coat. Tech*., 1995, **76-77**, 167-173.

25. Suvanto M., Raty J., Pakkanen T. A. Carbonyl‐precursor‐based W/Al_2O_3 and CoW/Al_2O_3 catalysts: characterization by temperature‐programmed methods, *Catal. Lett.*, 1999, **62**, 21–27.

26. Sun M., Xu N., Cao J.W., Yao J.N., Wang E.C., Nanocrystalline tungsten oxide thin film: Preparation, microstructure, and photochromic behavior, *J. Mater. Res.*, 2000, **15**, 927–933.

27. Brescacin E., Basato M., Tondello E. Amorphous WO_3 Films via Chemical Vapor Deposition from Metallorganic Precursors Containing Phosphorus Dopant, *Chem. Mater.*, 1999, **11**, 314–323.

28. Yu Z.R., Jia X.D., Du J.H., Zhang J.Y. Electrochromic WO_3 films prepared by a new electrodeposition method, *Sol. Energ. Mat. Sol. C.*, 2000, **64**, 55–63.

29. Krings L.H.M., Talen W. Wet chemical preparation and characterization of electrochromic WO_3, *Sol. Energ. Mat. Sol. C.*, 1998, **54**, 27–37.

30. Cheng W., Baudrin E., Dunn B., Zink J.L. Synthesis and electrochromic properties of mesoporous tungsten oxide, *J. Mater. Chem.*, 2001, **11**, 92–97.

31. Guo J.D., Li Y.J.J., Whittingham M.S. Hydrothermal synthesis of electrode materials Pyrochlore tungsten trioxide film, *J. Power Sources*, 1995, **54**, 461–464.

32. Mädler L., Liquid-fed aerosol reactors for one-step synthesis of nano-structured particles. *KONA*, 2004, **22**, 107-120.

33. Granqvist C.; Kish L.; and Marlow W., *Gas Phase Nanoparticle Synthesis*. London, England: Kluwer Academic Publishers, London, 2004.

34. Griffiths J.F.; and Barnard J.A., *Flame and Combustion, 3rd ed., Blackie*. London, England: Academic & Professional, London, 1995.

35. Wegner K., Stark W.J., Pratsinis S.E. Flame-nozzle synthesis of nanoparticles with closely controlled size, morphology and crystallinity, *Mater. Lett.* 2002, **55**, 318-321.

36. Kammler H.K., Mädler L., Pratsinis S.E. Flame synthesis of nanoparticles, *Chem. Eng. Technol.* 2001, **24**, 583-596.

37. Wegner K., Pratsinis S.E. Flame synthesis of nanoparticles, *Nanotechnology,* 2004, **6**, 27-29.

38. Gai, P.L., and Boyes, E.D., *Electron Microscopy in Heterogeneous Catalysis*, DuPont, Central Research and Development, Wilmington, DE, USA, Institute of Physics Publishing Bristol and Philadelphia, 2003.

39. Hodnett, B.K., *Heterogeneous Catalytic Oxidation: Fundamental and Technological Aspects of the Selective and Total Oxidation of Organic Compounds*, Department of Chemical and Environmental Sciences and The Materials and Surface Science Institute University of Limerick, Ireland, 2000.

40. Wetchakun, N., *Effect of Transition Metal Ion Doping on the Photocatalytic Activity of Titanium Dioxide*, Ph. D. Thesis, Chiang Mai University, Chiang Mai, Thailand, 2008.

41. Satterfield, C.N., *Heterogeneous Catalysis in Industrial Practice*. New York, USA: McGraw-Hill, New York, 1991.

42. Watt, I.M., *The Principles and practice of Electron Microscopy*., Cambridge University Press, Cambridge, 1997.

43. Egerton, R.F., *Physical Principles of Electron Microscopy; An Introduction to TEM, SEM, and AEM*, University of Alberta, Alberta, 2005.

44. Schiavello, M., *Heterogeneous Photocatalysis*, Wiley series in photoscience and photoengineering Vol. 3, Wiley, New York, 1997.

45. Gfroerer, T. M., *Photoluminescence in Analysis of Surfaces and Interfaces* Encyclopedia of Analytical Chemistry, Wiley, New York, 2000.

46. Liqiang J., Yichun Q., Baiqi W., Shudan L., Baojiang J., Libin Y., Wei F., Honggang F., Jiazhong S., Review of photoluminescence performance of nano-sized semiconductor materials and its relationships with photocatalytic activity, *Sol. Energ. Mat. Sol. C.*, 2006, **90**, 1773-1787.